3^{rd} harmonic ECRH absorption enhancement by 2^{nd} harmonic heating at the same frequency in a tokamak

S Gnesin[1], J Decker[2], S Coda[1], T P Goodman[1], Y Peysson[2], D Mazon[2]

[1]Ecole Polytechnique Fédérale de Lausanne (EPFL), Centre de Recherches en Physique des Plasmas (CRPP), Association Euratom–Confédération Suisse, EPFL SB CRPP, Station 13, CH–1015 Lausanne, Switzerland
[2]CEA, IRFM, F-13108 Saint-Paul-lez-Durance, France.

E-mail: `silvano.gnesin@epfl.ch`

Abstract.

The fundamental mechanisms responsible for the interplay and synergy between the absorption dynamics of extraordinary-mode electron cyclotron waves at two different harmonic resonances (the 2^{nd} and 3^{rd}) are investigated in the TCV tokamak. An enhanced 3^{rd} harmonic absorption in the presence of suprathermal electrons generated by 2^{nd} harmonic heating is predicted by Fokker-Planck simulations, subject to complex alignment requirements in both physical space and momentum space. The experimental signature for the $2^{nd}/3^{rd}$ harmonic synergy is sought through the suprathermal bremsstrahlung emission in the hard X-ray range of photon energy. Using a synthetic diagnostic, the emission variation due to synergy is calculated as a function of the injected power and of the radial transport of suprathermal electrons. It is concluded that in the present experimental setup a synergy signature has not been unambiguously detected. The detectability of the synergy is then discussed with respect to variations and uncertainties in the plasma density and effective charge in view of future optimised experiments.

1. Introduction

Electron cyclotron resonant heating (ECRH) has proven to be a reliable and efficient tool for heating and current drive in magnetically confined plasma devices [1, 2, 3]. Its efficient plasma coupling and intrinsically localized power deposition make it particularly suited for the stabilisation and control of various MHD instabilities in present fusion devices and future ones such as the ITER tokamak [4, 5].

In the case of high power-density EC wave absorption, the electron distribution function can become substantially distorted from the equilibrium Maxwellian shape. As a consequence, the assumptions of linear wave-coupling theory are no longer valid and a kinetic description of the wave absorption mechanism becomes necessary. The quasilinear Fokker-Planck formalism is the most commonly applied tool for these conditions. It accounts for suprathermal electron generation and for the nonlinear flattening of the distribution function, both of which affect wave absorption. The effect of fast electron transport can also be incorporated.

On the TCV tokamak a number of fundamental studies of EC wave-plasma coupling have been performed over the years [6, 7], including the role of electron transport in regulating the driven current, through direct measurements as well as Fokker-Planck modelling [8, 9]. The TCV tokamak offers also the ability to deposit EC power at different harmonics simultaneously in the same plasma. This opens the possibility for novel investigations into the fundamental physics of wave-plasma interaction, both experimental and theoretical, which are the object of the present work. The primary simulation tool employed here is the recently developed Fokker-Planck code LUKE [10].

The TCV tokamak (major and minor radii $R = 0.88$ and $a = 0.25$ m, magnetic field up to 1.5 T, plasma current up to 1.0 MA) [11] is equipped with nine electron cyclotron wave sources: six 0.5-MW gyrotrons at $f = 82.7$ GHz usually employed for ECRH at the 2^{nd} harmonic in the extraordinary mode (X2), and three 0.5-MW gyrotrons at $f = 118$ GHz usually employed for 3^{rd} harmonic ECRH, also in the extraordinary mode (X3) [12]. Thus TCV is ideally suited for the study of high power-density EC heating and current drive (ECCD) with the possibility to inject X2 and X3 EC waves simultaneously. The X2 and X3 gyrotron frequencies are designed to place the two EC resonances near the magnetic axis at the nominal magnetic field (1.45 T).

X3 heating in particular enables access to high density plasmas (up to $n_e = 1.1 \times 10^{20}$ m^{-3}), whereas X2 is cut off from the plasma for $n_e > 4.3 \times 10^{19}$ m^{-3}. Since the plasma is optically thin for the 3^{rd} harmonic, the X3 wave is usually injected vertically from the top of the machine in order to align the ray path with the resonant surface and thus maximize the total first-pass absorption by the plasma. X2 injection is effected by means of two clusters of three beams each, launched from the low-field side (LFS) of the vessel. Each beam can be independently oriented in real time providing either co- or counter-current toroidal injection and the possibility to control the radial deposition location in the poloidal plasma cross section. Since the plasma is optically thick to X2 radiation under most conditions, this arrangement allows localized heating

at any radial location in virtually all geometries.

Early experiments with simultaneous X2 and X3 injection were performed in TCV with X3 also injected from a LFS launcher [13]. More recently, several experiments have benefited from simultaneous X2 and (top-launched) X3 heating. However, simultaneous injection at the nominal X2 and X3 frequencies is not the only way to achieve and study combined 2nd and 3rd harmonic wave absorption in TCV. By decreasing the toroidal magnetic field and using only the 82.7 GHz gyrotrons, we can obtain magnetic configurations in which both the 2nd and 3rd harmonic resonant layers are present in the plasma at the same time for the same EC wave frequency. TCV experiments were expressly devised by one of the authors (T.P.G.) to explore this idea and, in particular, to study the influence of 2nd harmonic heating on 3rd harmonic wave absorption. Power injection was effected exclusively through LFS launchers at 82.7 GHz.

The interpretation of the experimental results through comparison with numerical simulations is the object of this work. Synergistic effects are indeed predicted by the analysis, both in the power absorption efficiency and in the hard X-ray bremsstrahlung emission. We find, however, that once all parametric dependences are normalized out, no evidence of synergy can be gleaned from the data: this is consistent with the theoretical prediction that synergistic variations are smaller than both the experimental error bars and the uncertainties from unknown model parameters.

The experimental setup is outlined in section 2, followed by a description of the main diagnostic tool, a hard X-ray camera, in section 3. The modelling of this experiment is performed with the LUKE Fokker-Planck code, presented in section 4. An overview of the experimental results follows in section 5. Since a magnetic-field sweep is the clearest and most direct way to explore the possible synergy and its experimental signatures, an extensive numerical analysis is presented in section 6 of an especially representative discharge featuring such a sweep. The interested reader will find further details of the analysis in Appendix A. The perspectives for the detection of synergy, including its parametric dependences, are examined in section 7. Conclusive remarks are offered in section 8.

2. Experimental setup

We performed a set of experiments with up to 1 MW EC power from two 82.7 GHz gyrotrons injected from the LFS. By varying the toroidal magnetic field B_0 while keeping the beam injection geometry constant, it is possible to move the deposited power location along the major radius, shifting it towards the LFS or HFS of the device. In TCV, there exists a range of B_0 values for which both the 2nd and 3rd harmonic cold-plasma resonant surfaces are present in the plasma simultaneously for that same frequency. Moreover, for a particular value of B_0 both resonances can be made to lie on the same flux surface. In particular, by gradually decreasing the toroidal magnetic field during the discharge, one can ensure that this combined 2nd and 3rd harmonic heating on the same flux surface will occur at some time t_X during the discharge. This procedure is visualized in figure 1

where $t_X \simeq 1.3$ s.

Ideally, as in all studies of synergistic effects, one would wish to compare cases with and without synergy, under the same experimental conditions. However, the experimental setup clearly precludes this possibility. A magnetic-field sweep therefore appears to be the simplest and clearest means to seek a synergy signature. One must be mindful, however, that conditions charge drastically during such a sweep, most notably the wave's absorbed power fraction. A sensitivity study will therefore be an essential component of this analysis.

The goal of the study is to determine the effect, if any, of 2nd harmonic heating on 3rd harmonic absorption. In the remainder of this paper we shall refer to this effect as "synergy" or "synergistic absorption"; the synergy will be positive if 3rd harmonic absorption increases relative to the level with no 2nd harmonic heating, negative in the opposite case. The expectation, guided also by previous results [13], is that a positive synergy would be mediated by a suprathermal electron population generated by 2nd harmonic wave-plasma interaction. A significant suprathermal population is invariably observed whenever 2nd harmonic waves are injected in ECCD mode, i.e., with a finite parallel wave number [6, 14]. For this reason, the EC beams in the experiment under discussion were injected with a 16^o toroidal angle.

Because of the far off-axis location of the power deposition and the intrinsically poor 3rd harmonic absorption efficiency (the deposited power fraction being of order 1%), any enhancement in the latter is not measurable by a direct power absorption measurement technique (e.g. through the response of the stored energy to modulated ECRH [15]). However, an indirect indication of a possible synergistic effect on the 3rd harmonic absorption could be provided by variations in the signal measured by suprathermal electron diagnostics [16]. On TCV two such diagnostics were available during these experiments: a high-field-side electron cyclotron emission (ECE) radiometer and a vertically viewing, 14-chord hard X-ray (HXR) camera [17]. Interpretation of the ECE data is complicated by the lack of localization, as each detection frequency corresponds to a finite range of energies and positions. We have therefore focused on the spatially resolved HXR camera, which is discussed in the next section.

3. Diagnostic tool: the HXR camera

The most relevant experimental information is provided by a HXR diagnostic [17, 18], measuring bremsstrahlung emission by suprathermal electrons. This consists of a multi-detector camera that has been employed on TCV, on loan from CEA-IRFM‡, for several experimental campaigns between 1998 and 2009. The camera employs 21 CdTe detectors (5×5 mm$^2 \times 2$ mm thick) viewing the plasma vertically in a fan arrangement through a 5×5 mm^2 square pinhole collimator and a 0.25-mm thick beryllium window. Since the camera was not expressly designed for TCV, only 14 detectors (#5 through #18)

‡ Commissariat à l'Energie Atomique et aux Energies Alternatives, Institut de Recherche sur la Fusion Magnétique

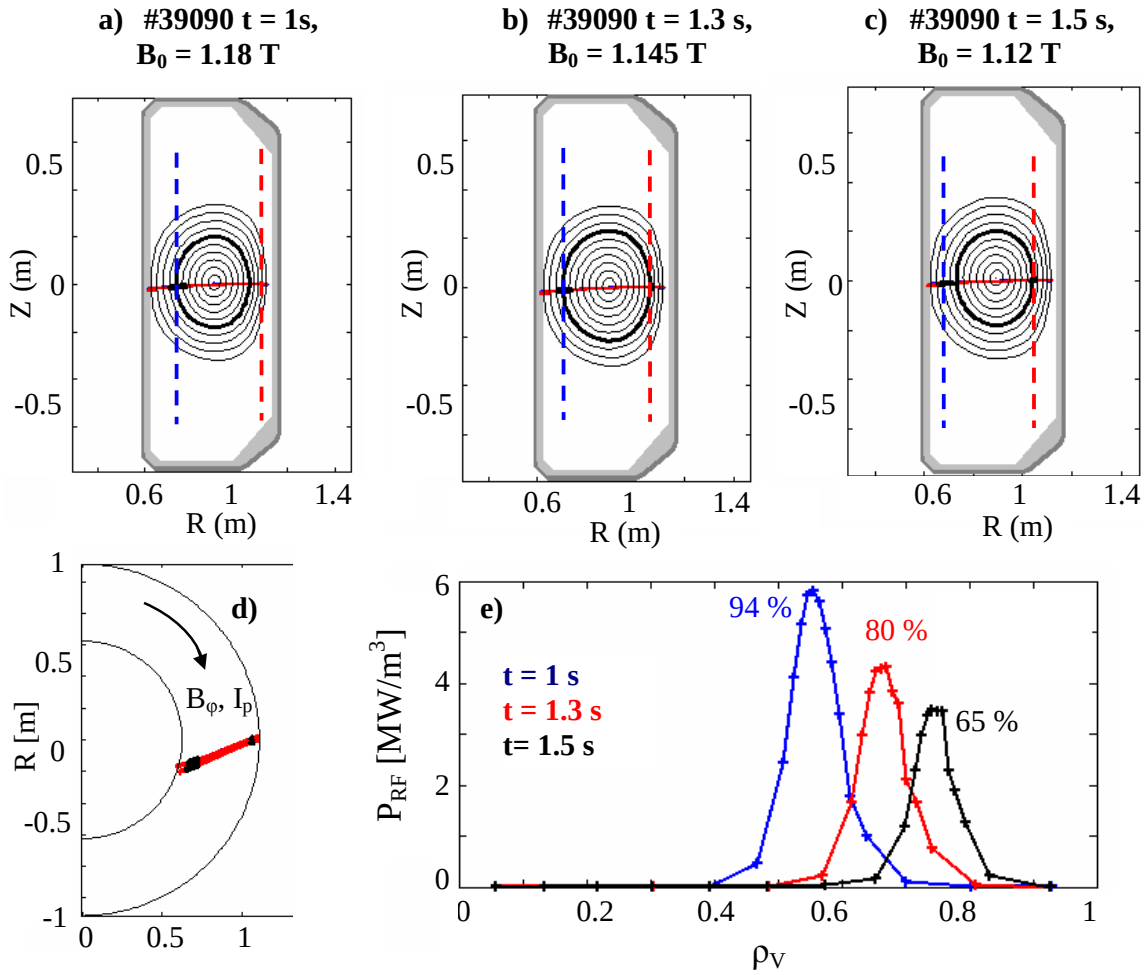

Figure 1. (a)-(c) Time evolution of the magnetic plasma configuration during a decreasing magnetic sweep in the TCV shot 39090. The cold-plasma 2nd and 3rd resonances are depicted by vertical blue and red dashed lines, respectively. The two resonances lie on the same flux surface at $t = 1.3$ s, represented by the thick black curve. (d) Top view of C3PO ray tracing: two 0.5-MW, 82.7-GHz ECRH beams are injected from the LFS with a 16^o toroidal angle in counter-current configuration (in the case shown). The cold 2nd and 3rd harmonic resonant layers move to smaller major radii with time. The dominant 2nd harmonic absorption region moves away from the magnetic axis (on the plasma HFS) while the 3rd harmonic absorption region moves toward the center (on the LFS). (e) Radial power deposition profiles generated by the C3PO/LUKE ray-tracing and Fokker-Planck code suite for 3 time slices: $t = 1.0$ s, $t = 1.3$ s and $t = 1.5$ s. The fraction of absorbed power ($P_{\rm abs}/P_{\rm inj}$) for each time slice is indicated near each absorption peak. The radial coordinate here is the square root of the normalized volume (ρ_V) enclosed by a given flux surface.

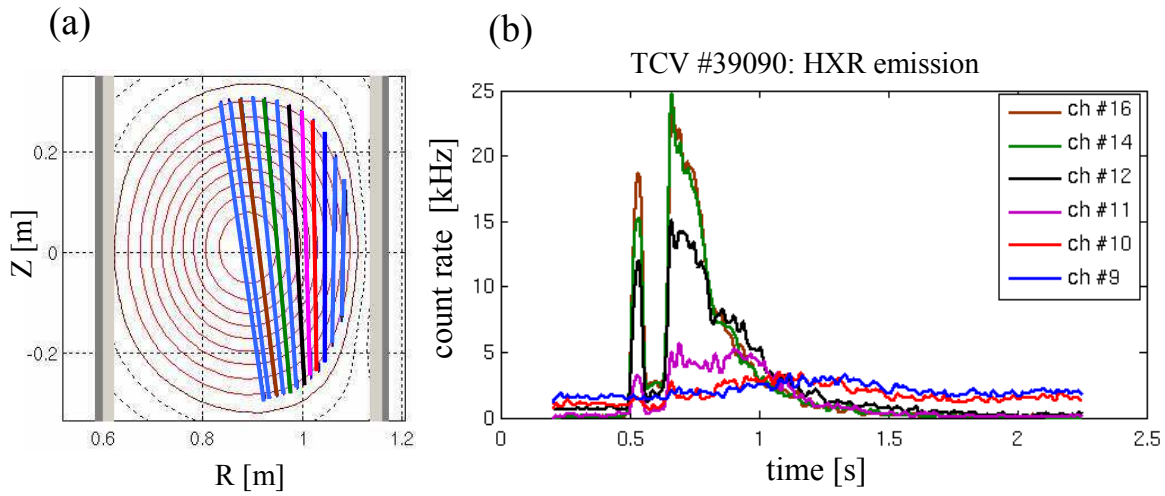

Figure 2. (a) Vertically viewing HXR camera geometry on TCV shot 39090. Only chords #7–#18, shown in the picture, view the plasma (#7 is the rightmost and #18 the leftmost). (b) Non thermal bremsstrahlung emission in the 16–40 keV energy range as a function of time for selected chords.

have a complete or partial view of the plasma, and of these #5 and #6 are generally excluded from the analysis because of parasitic thick-target emission from the outer wall. Detectors #7 to #18 (#7 being at the periphery and #18 at the center) provide a complete radial coverage of the LFS half of the plasma poloidal cross section, plus a small fraction of the HFS (figure 2(a)). Shielding against uncollimated radiation is provided by a 2-cm lead casing sandwiched between two 0.25-cm thick plates of stainless steel.

The detector signal is processed by a charge preamplifier followed by a Gaussian pulse shaping amplifier. Pulse height spectroscopy is performed by splitting each signal 8 ways to feed 8 analog variable-threshold discriminators. The end result is a set of time traces of photon counts for 8 energy bins (the highest of which has no upper bound) for each chord. The energy thresholds can be set before each discharge. Stainless steel absorbers of varying thickness can also be inserted between discharges to reduce the flux and avoid counting saturation.

4. The LUKE Fokker-Planck code

Linear ray-tracing codes calculate the wave absorption by assuming a Maxwellian background distribution function. Therefore, this treatment cannot account for effects due to the presence of suprathermal electrons accelerated by the waves. Variations in the 3rd harmonic absorption due to the presence of 2nd harmonic power deposition in this framework can thus only emerge as an indirect effect caused by variations in the electron temperature and density.

To explore the synergy effect, the Fokker-Planck solver LUKE [10] is used in this

paper. This fully linearized, relativistic 3D bounce-averaged Fokker-Planck solver is coupled with the C3PO ray tracing [19] and R5-X2 bremsstrahlung codes [20]. The R5-X2 module provides us with a synthetic HXR diagnostic, implemented with the specific geometry of the HXR camera installed on TCV. The code takes as input data the magnetic equilibrium of a given TCV shot, reconstructed by the LIUQE code [21], as well as the EC wave launching parameters (total injected power, mirror angles, wave polarization), the electron temperature and density profiles measured by Thomson scattering, the ion temperature profile measured by charge exchange recombination spectroscopy, and the effective charge (Z_{eff}) derived by a soft X-ray diagnostic. In standard simulations Z_{eff} is assumed to be spatially uniform.

The LUKE code accounts for the effect of an applied electric field (inductive loop voltage). Written in a fully conservative form, the code naturally conserves the electron density as well as momentum for the correct treatment of the current drive problem. The key LUKE output of interest in this study is the total absorbed power, along with the fraction of power absorbed at each individual harmonic treated by a given simulation. In addition, a number of quantities are made available in output to help elucidate the details of the underlying physics: these include the ECRH diffusion tensor (D_{RF}), the collision operator and the distribution function.

The Fokker-Planck equation is solved in a time-scale frame, where the magnetic field is assumed to be large enough that the electron gyro-motion angular period $\Omega^{-1} = [eB/(m_e\gamma)]^{-1}$ is much shorter than the collision time τ_c and bounce time τ_b. The electrons are considered to remain on a given flux surface for a time long compared to the poloidal electron bounce time; this condition is equivalent to writing: $\tau_b \ll \tau_c, \tau_d, \tau_f$, where τ_d and τ_f are the radial electron drift time and the characteristic time of fast electron radial transport, respectively. Furthermore, the radial electron drifts are neglected ($\tau_c \ll \tau_d$) and trapped electrons are assumed to perform several bounce motions before being scattered out of the trapped region by Coulomb collisions (low collisionality regime). These assumptions can be summarized in the following time ordering:

$$\Omega^{-1} \ll \tau_b \ll \tau_c \ll \tau_d \simeq \tau_f \ll \tau_{eq}, \tag{1}$$

where τ_{eq} is the equilibrium evolution time scale. The Fokker-Planck equation is evaluated on a 3-D (ψ: radial, p: momentum, ξ_0: pitch angle coordinate) space grid [22] and takes the form of a continuity equation for the electron distribution function f:

$$\frac{df}{dt} = \frac{\partial f}{\partial t} + \nabla \cdot S = s_+ - s_-, \tag{2}$$

where s_+ and s_- are the local bounce-averaged external source and sink terms respectively. The particle flux S can be expressed as the sum of a diffusive (D) and a convective (F) contribution

$$S = -D \cdot \nabla_{(\psi,p,\epsilon_0)} f + Ff \tag{3}$$

where flux induced by collisions, electric field convection, RF diffusion in velocity space and radial transport are included. The non linearity in wave power absorption calculations is contained in the relativistic RF diffusive term

$$S_{RF} = -D_{RF} \cdot \nabla_p f. \tag{4}$$

The code offers the possibility to incorporate any type of fast electron radial transport (collision, turbulence or wave induced), which is a key ingredient for the correct calculation of local plasma properties such as the driven current density [8]. Arbitrary radial diffusion ($D_{\psi\psi}$) and convection (F_ψ) terms can be handled and integrated in an expression for the flux:

$$S_T = -D_{\psi\psi}\nabla f + F_\psi f \tag{5}$$

Two types of radial transport diffusion coefficients are currently implemented [10] to model two particular mechanisms believed to be responsible for anomalous radial electron transport:

(i) Electrostatic-fluctuation induced transport (ES): fast electrons with normalized parallel velocity exceeding a given threshold ($v_{e\|}$) diffuse radially with a constant radial diffusion coefficient ($D_{\psi\psi 0}$ [$\mathrm{m^2 s^{-1}}$]) that can be set by the user

(ii) Electromagnetic-fluctuation induced transport (EM): this form of turbulence causes a radial fast electron diffusion coefficient proportional to the parallel electron velocity: $D_{EM} \propto v_{e\|}$.

The bremsstrahlung code R5-X2 is included in LUKE and plays the role of a synthetic diagnostic, incorporating in particular the geometry of the HXR vertically viewing camera. For each simulation, a calculation of the line integrated HXR signal, for each line of sight, is provided. A detailed treatment of the non-thermal bremsstrahlung calculation can be found in [20].

5. Experimental results

An initial set of exploratory experiments were performed on TCV in 2003 to probe the synergy effect. An example (shot 25474) is shown in figure 3. The measured HXR signal showed a maximum in coincidence with the crossing time ($t_X = 0.9$ s), suggestive of a synergy signature. This time however also coincides with a minimum in density (figure 3). Subsequent Fokker-Planck analysis showed that the HXR peak is due to the density dip rather than to a synergy effect. These dependences will be discussed in detail in the next two sections. The limited machine time allotted to this experiment at the time did not allow for a refinement of the density control, which has been generally difficult in TCV in the past in cases of time-varying plasma conditions, as it relied on simple PID control of a gas valve without any active cryopumping.

It is also found that a significant fraction of the HXR signal appears in the uppermost range of the measured energy spectrum ($E_\gamma > 64$ keV); this component

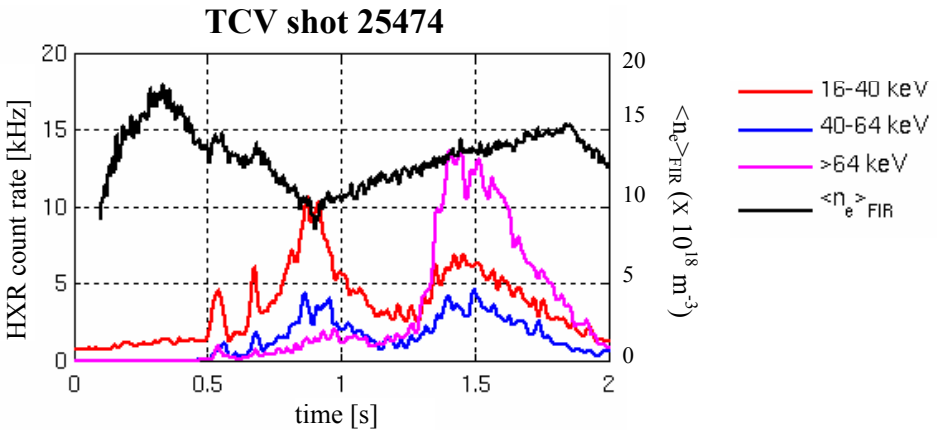

Figure 3. TCV discharge 25474: non-thermal bremsstrahlung emission as a function of time in the (red) 16–40 keV, (blue) 40–64 keV and (magenta) >64 keV energy ranges on chord #12 (mid-radius) of the vertically viewing HXR camera. The line-averaged electron density is shown in black.

indeed becomes dominant for $t > 1.3$ s in the case shown in figure 3. These highly energetic transients are visible also in signals from HXR detectors without a direct view of the plasma, as well as from a heavily shielded scintillator-photomultiplier system that measures the flux of hard X-rays escaping the TCV walls. This phenomenology is clearly related to significant runaway electron activity, resulting in thick-target bremsstrahlung emission up to the MeV range.

Based on these initial results and on the subsequent numerical analysis, a new series of plasma discharges have been performed recently with the goal of achieving better density control and of suppressing the runaway electron generation. The TCV shot 39090 is a particularly representative shot for the present study and will therefore be discussed at some length. All the salient features of the basic physical mechanisms at play are found in this particular discharge. A limited plasma (elongation $\kappa = 1.3$, triangularity $\delta = 0.12$) is centered 8 cm above the equatorial plane of the machine, in front of the two equatorial ECRH launchers. The toroidal magnetic field is decreased during the discharge from $B_1 = 1.23$ T at $t = 0.5$ s to $B_2 = 1.07$ T at $t = 1.9$ s. The magnetic configurations for three consecutive time slices ($t = 1.0, 1.3, 1.5$ s, respectively) are plotted in figure 1. At $t_X = 1.3$ s the cold 2^{nd} and 3^{rd} harmonic resonances cross the same flux surface (figure 1(b)). The total plasma current is adjusted during the magnetic field ramp in order to keep the edge safety factor constant. The plasma is shaped to minimise the width of the radial power deposition profile by imposing nearly vertically straight flux surfaces in the equatorial plane (matching the EC resonant surfaces which are also vertically straight), where the EC power absorption occurs for both harmonics. Two EC beams (450 kW each) are injected equatorially from the LFS so that their poloidal projections cross the magnetic flux surfaces perpendicularly. The toroidal injection angle is $\phi = 16^o$. The EC power is injected from 0.5 to 2.0 s with two modulation phases for 0.55 s $\leq t \leq$ 0.65 s and 1.85 s $\leq t \leq$ 1.95 s. The current is

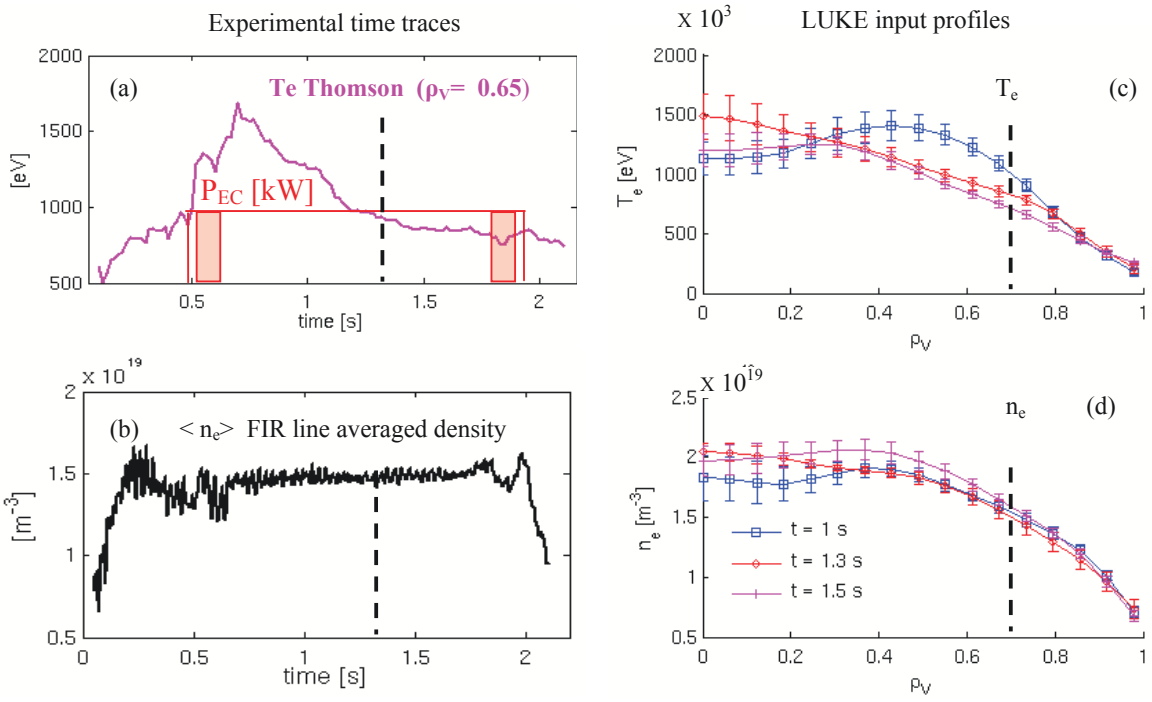

Figure 4. Time traces of the electron (a) temperature at the location where the 2nd and 3rd harmonic resonances cross, and (b) line-averaged density in shot 39090, from the Thomson scattering and FIR diagnostics, respectively; the dashed vertical lines denote the time at which the cold 2nd and 3rd harmonic resonances coincide. Fitted LUKE input profiles of (c) temperature and (d) density for three different times; the dashed vertical lines indicate the location of the two cold resonances at the crossing time $t_X = 1.3$ s.. The injected EC power is also shown in (a).

sustained primarily by the transformer ($V_{\rm loop} \neq 0$) with only a minor contribution(<5%) from ECCD.

In figure 4(a) we show the injected EC power, as well as the electron temperature T_e, measured by a Thomson scattering diagnostic at the radial location where absorption occurs when the 2nd and 3rd harmonic resonances lie on the same flux surface. The temperature decreases in time as the dominant 2nd harmonic absorption moves off-axis. The absorbed power is 100% near the beginning ($t = 0.7$ s) of the unmodulated EC injection phase, is still 80% at $t = 1.3$ s and decreases to ∼60% at $t = 1.5$ s (figure 1(e)). The line-averaged density measured by a far infrared (FIR) interferometer is 1.5×10^{19} m^{-3} during the entire EC phase, with fluctuations of less than 10% in the 0.7–1.8 s time interval (figure 4(b)). The temperature and density profiles from Thomson scattering are shown for our three times in Figs. 4c and 4d. The density profiles vary little with time (<5%) in the radial region of interest for the EC wave absorption ($0.4 \leq \rho_V \leq 0.9$, see figure 1(e)).

The HXR emission in the 16–40 keV range is shown in figure 2(b) for selected chords from the core (#16) to the edge (#9). In the course of the magnetic-field sweep, the HXR emission is seen to decrease generally with time. This tendency is understood

to be due to the dominant X2 absorption moving to the periphery, which results in a decrease in the absorption fraction (figure 1(e)) and in the electron temperature (figure 4(c)). Additionally, the flux-surface averaged density of EC power deposition decreases intrinsically as the X2 absorption moves to the periphery, since the flux-surface area increases. This results in a decrease in the quasilinear effects, in the suprathermal electron generation and, consequently, in the HXR emission.

An experimental signature of synergy between 2$^{\text{nd}}$ and 3$^{\text{rd}}$ harmonic absorption, when the two resonances are correctly aligned, would be expected to take the form of a variation of the HXR signal running contrary to the macroscopic trends just described. For instance, a minor local peak is seen in the time traces on chords 11 and 12 at $t = 0.9$ s, on chord 10 at 1.1 s and on chord 9 at 1.3 s (figure 2(b)). A numerical analysis, based on Fokker-Planck calculations - which account for the synergy - and a HXR synthetic diagnostic are required to determine if these variations are due to synergistic effects. This is the objective of the remainder of this paper.

6. Numerical modelling of the experiment

In this section we shall proceed as follows. In a first stage we present the numerical study of the synergy in the 3$^{\text{rd}}$ harmonic power absorption. We subsequently compare the experimental HXR profiles to the calculated ones, and study how the free parameters in the modelling must be adjusted to optimise the matching. With this knowledge in hand, we then proceed to investigate the possible experimental signatures of synergy suggested in section 5, i.e., the nonmonotonic behaviour and the local peaks in the HXR time traces. We use the numerical tools to determine whether these features are due to synergy or to other causes.

6.1. Synergistic effects in power absorption

Two definitions of synergy are used in the numerical simulations:

(i) a relative figure of merit $R_3 = \chi_3^{[1,2,3]}/\chi_3^{[3]}$ where $\chi_3^{[1,2,3]} = P_3^{[1,2,3]}/P_0$ and $\chi_3^{[3]} = P_3^{[3]}/P_0$, and $P_3^{[1,2,3]}$ is the power absorbed at the 3$^{\text{rd}}$ harmonic calculated when all harmonics (fundamental, 2$^{\text{nd}}$ and 3$^{\text{rd}}$ harmonic) are taken into account in the Fokker-Planck simulation, whereas $P_3^{[3]}$ is the absorbed power when only the 3$^{\text{rd}}$ harmonic is considered, and P_0 is the total injected power. The quantities $P_3^{[1,2,3]}$ and $P_3^{[3]}$ are provided in output by each LUKE run.

(ii) the absolute figure of merit $S_3 = \chi_3^{[1,2,3]} - \chi_3^{[3]}$.

Synergy is present when $R_3 > 1$ and $S_3 > 0$, whereas $R_3 = 1$ and $S_3 = 0$ indicate no synergistic enhancement.

In the course of the magnetic-field ramp in shot 39090 the following sequence occurs. Initially the nominal (cold) 2$^{\text{nd}}$ harmonic resonance occurs well in the plasma core, whereas the cold 3$^{\text{rd}}$ harmonic resonance is outside the plasma to the LFS. The only electrons that can be resonant at the 3$^{\text{rd}}$ harmonic under these conditions are those with

very high energy located near the outer edge of the plasma, with strongly relativistically down-shifted cyclotron frequency. As time advances, the 2nd harmonic resonance moves towards the HFS edge while progressively lower energy electrons become resonant at the 3rd harmonic, until the cold resonance enters the plasma. The two nominal resonances coincide at $\rho \sim 0.7$ at $t = 1.3$ s. At later times, the 3rd harmonic resonance is at a smaller minor radius than the 2nd harmonic one.

A series of simulations have been performed to cover the EC phase between 0.7 and 1.5 s with a 0.05-s time step or less where necessary. The experimental profiles (n_e, T_e, $Z_{\rm eff}$) and the magnetic equilibria given as inputs to the code are averaged over 40-ms time intervals. The constancy of the electron density is a key point in the present analysis, as this is a plasma parameter to which both the synergy and the HXR emission are extremely sensitive. A 10% fluctuation in the electron density corresponds to a ∼30% variation in the expected HXR emission from LUKE/R5-X2 simulations. For each time slice, simulations with all harmonics (fundamental, 2nd and 3rd), with the 2nd harmonic alone and with the 3rd harmonic alone were performed; crucially, in each case the individual contribution of each harmonic to the total absorbed power is generated by the code. It should be noted that the contribution of the fundamental mode has proven to be negligible ($P_{\rm abs}^{\rm 1^{st}harm}/P_{\rm abs}^{\rm tot} \sim 10^{-6}$) in all the cases analysed; accordingly, the plots shown in the remainder of this work will not include the fundamental mode dynamics. The simulations were performed first with no fast electron radial diffusion ($D_{ES} = 0$) and were then repeated with $D_{ES} = 0.5$ m^2/s.

The radial profiles of the EC power deposition generated by LUKE are shown in figure 5 for the case without diffusion. The outward movement of the 2nd harmonic absorption region due to the magnetic-field sweep is clearly seen in the right-hand column. It is also clear that the (very faint) 3rd harmonic absorption has a negligible influence on the 2nd harmonic absorption. In the left-hand column the bulk 3rd harmonic absorption is seen to enter the plasma at approximately 1 s. In addition, however, there is evidence for synergistic 3rd harmonic absorption well before this time, which translates into very high values of R_3 (due to the smallness of the denominator) as shown in figure 6(a). This "anomalous" absorption is radially aligned with the peak of the 2nd harmonic absorption.

The absolute synergy ratio is shown in figure 6(b) and is seen to decrease very slightly over the 0.73–1.2 s time window, followed by a slight peak at $t = 1.3$ s, the 2nd /3rd harmonic crossing time (t_X); a sharp drop is observed after this time. The effects of a suprathermal diffusivity $D_{ES} = 0.5$ m^2/s are minor and do not alter this temporal dependence.

These synergy dynamics are analysed in detail in Appendix A. Not surpringly, it is found that significant synergy occurs when appropriate matching conditions are met between the 2nd and 3rd harmonic resonances in radial and energy spaces, along with the generation of a large population of suprathermal electrons at the phase space location where the match is obtained. At times t< 1.3 s, the resonant region satisfying the matching conditions in radial and energy spaces is located on the LFS of the nominal,

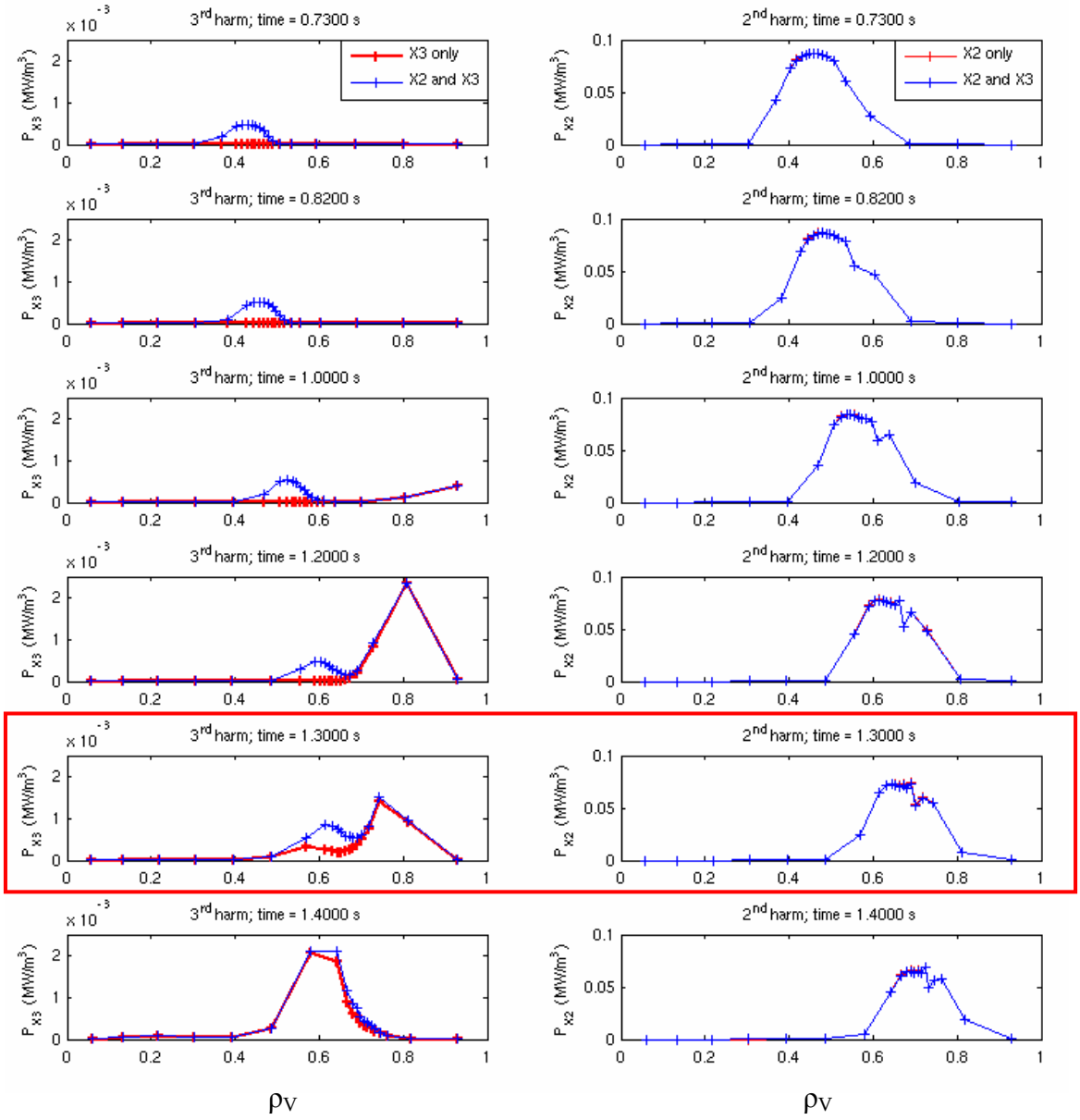

Figure 5. TCV shot 39090: the radial power deposition profiles produced by the LUKE FP code for different time slices in the 0.7–1.5 s interval; the box highlights the crossing time $t_X = 1.3$ s. The left column depicts the power absorbed at the 3rd harmonic both when the other harmonics are neglected (red) and when they are taken into account (blue); the equivalent plots for the 2nd harmonic are on the right. Note the large difference in the absolute power density values between the two columns. Here radial fast electron diffusion is assumed to be absent.

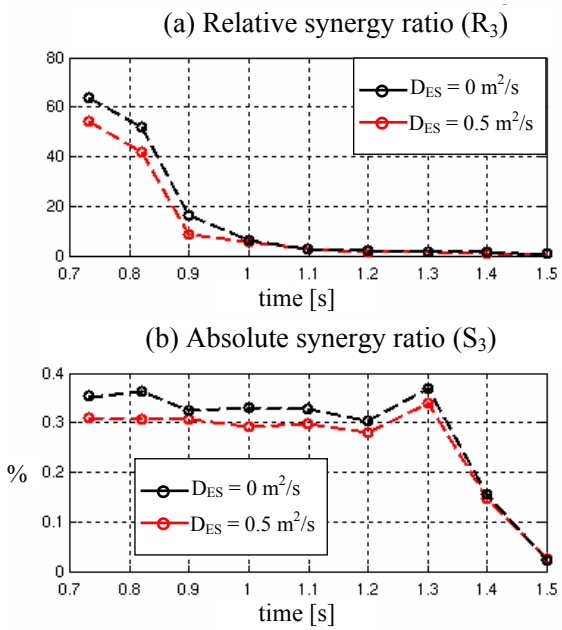

Figure 6. (a) Relative R_3 and (b) absolute S_3 figures of merit for the synergy (TCV shot 39090), without radial transport (black curves) and with radial suprathermal-electron diffusivity 0.5 m^2/s (red curves)

cold 2$^{\text{nd}}$ harmonic resonance, where a large population of suprathermal electrons is generated. At times t> 1.3 s, the matching resonance is located on the HFS of the cold 2$^{\text{nd}}$ harmonic resonance, where the generation of suprathermal electrons is limited, such that the synergistic 3$^{\text{rd}}$ harmonic absorption is smaller.

It should be pointed out that electrons resonating at the 2$^{\text{nd}}$ and 3$^{\text{rd}}$ harmonics have typically very different equatorial pitch angles, as the 2$^{\text{nd}}$ harmonic resonance occurs on the HFS where the EC wave interacts mainly with circulating electrons, while the 3$^{\text{rd}}$ harmonic resonance takes place on the LFS where it mostly involves trapped electrons. Yet, the high level of pitch-angle scattering, aided by a high effective charge, ensures an efficient redistribution of the suprathermal population across all pitch angles, such that synergistic effects can still be significant.

6.2. Experimental HXR emission profiles vs numerical simulations

Here, we compare the HXR experimental signal from the vertically viewing camera with the simulated line integrated signal generated by the LUKE/R5-X2 bremsstrahlung calculator, and adjust the free parameters in the simulation to optimise the matching. The measured HXR emission is concentrated in the 16-40 keV energy range (see figure 7); photon statistics become poor at higher energy. Runaway generation is suppressed by adequate density control (cf. figure 3). We ignore the energies below 16 keV because the signal here can still be dominated by thermal bulk emission and is also more distorted by Compton scattering [20]. The HXR signals, like all the input data to the simulations,

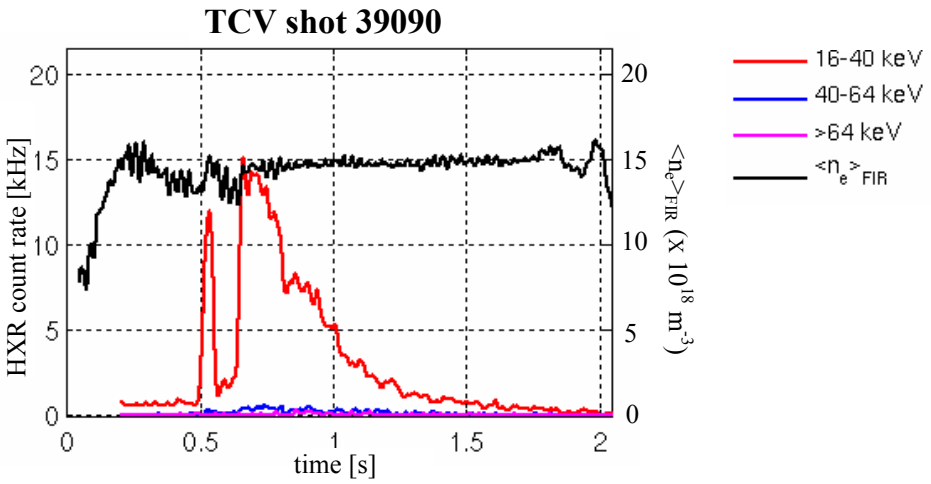

Figure 7. TCV discharge 39090: non-thermal bremsstrahlung emission as a function of time in the (red) 16–40 keV, (blue) 40–64 keV and (magenta) >64 keV energy ranges on chord #12 (mid-radius) of the vertically viewing HXR camera. The line-averaged electron density is shown in black.

are averaged over 40-ms intervals.

The experimental HXR signal in the TCV shot 39090 decreases with time as the 2nd harmonic absorption moves off-axis as a consequence of the decreasing B field. This behaviour is well reproduced by simulations (figure 8) and is due to the decrease in power absorption as the resonance moves off-axis. The quantitative agreement is also fair, to within 30% on all chords. However, a systematic mismatch is found in the shape of the profile (signal vs chord number): in the early EC phase ($t < 0.9$ s), the experimental profile peaks in the center (chords 16–17) whereas the simulated profile peaks off-axis (chord 11).

While a ∼30% agreement can be considered acceptable, we may ask whether tuning the transport coefficients might improve the match further. In particular, we expect a higher level of fast electron radial transport to help: it is even possible for radial diffusion to result in a centrally peaked HXR emission profile in the presence of off-axis heating, depending on the details of the phase-space dynamics [23]. Indeed, a better agreement at mid-radius is obtained with $D_{ES} = 2$ m^2/s at $t = 0.8$ s, and $D_{ES} = 1$ m^2/s at $t = 0.9$ s (the optimum level of radial transport increasing with the absorbed EC power); however, the central HXR level is not recovered, nor is a central peak observed, even when imposing an unrealistic $D_{ES} \sim 10$ m^2/s. An excellent agreement between experiment and simulation is obtained instead at $t = 0.8$ s by adding a convective term (F_ψ) with a strong radial pinch $V_{r0} = -60$ m/s (figure 9). It is worth noting, once again, that even such a strong convection does not influence significantly the value of the total current predicted by the FP code. For $0.9 < t < 1$ s, a radial diffusivity of 1 m^2/s is sufficient to reproduce the experimental results without the need for a convection term. Finally for $t > 1$ s when the dominant 2nd harmonic power deposition moves further off-axis, an outward convection ($V_{r0} > 0$) of typically 20 m/s along with a

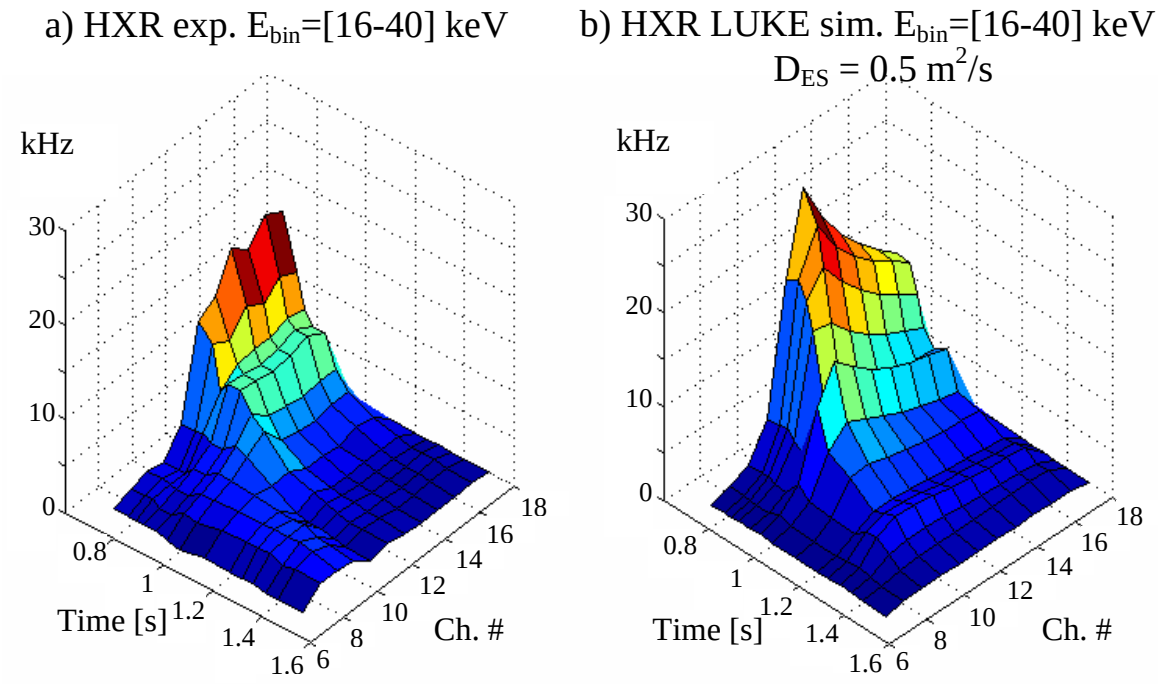

Figure 8. Shot 39090: HXR signal vs chord number in the energy range 16–40 keV: (a) experimental data from HXR camera, (b) simulation results from LUKE/R5-X2 ($D_{ES} = 0.5$ m^2/ s).

modest radial diffusion of $D_{ES} = 0.5$ m^2/s would be needed for an optimal match with the experimental HXR radial profile.

It may also be asked whether the experimental value of the plasma current provides a constraint on the value of the diffusivity. The constraint is found to be rather weak, since the plasma current is primarily carried by the Ohmic component and is therefore little affected by fast electron diffusion (figure 10). The total current calculated by LUKE is determined primarily by the plasma resistivity and thus depends strongly on $Z_{\rm eff}$ (figure 10), which in turn is known experimentally only with modest precision. The value of $Z_{\rm eff}$ necessary to reproduce the experimental current is compatible, within the error bars, with the experimental value of $Z_{\rm eff}$ provided by a soft X-ray diagnostic, which averages at 3 (with ∼20% fluctuations) during the discharge.

On the other hand, the strong constraint exerted on $Z_{\rm eff}$ by the total plasma current value precludes the utilisation of $Z_{\rm eff}$ or its profile as a free parameter in the simulations. For instance, to reproduce the central peaked HXR profile at $t = 0.8$ s a Gaussian radial profile peaking at $Z_{\rm eff} = 12$ in the plasma center and rapidly decreasing to 1.5 at $\rho_V = 0.5$ would be required, giving rise to a total calculated current of 442 kA, incompatible with the experimental value of 240 kA. When the same exercise is repeated at $t = 1.3$ s with a flat $Z_{\rm eff} = 2.5$ radial profile, the result is a value of $I_p = 300$ kA that is $\sim 25\%$ more than the experimental value.

To quantify the variation of the HXR signal due to the synergy we define the

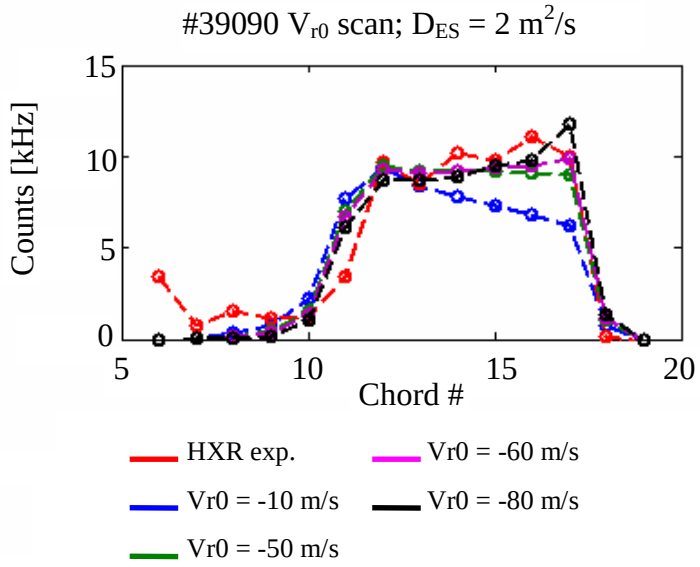

Figure 9. TCV shot 39090, $t = 0.8$ s. Influence of inward convection ($V_{r0} < 0$) on the predicted LUKE/R5-X2 HXR level in the energy range 16–40 keV. The experimental HXR level (curve in red) on chords viewing the plasma core (14-17) is best reproduced by adopting $V_{r0} = -60$ m/s (magenta curve). In these simulations $D_{ES} = 2$ m^2/s.

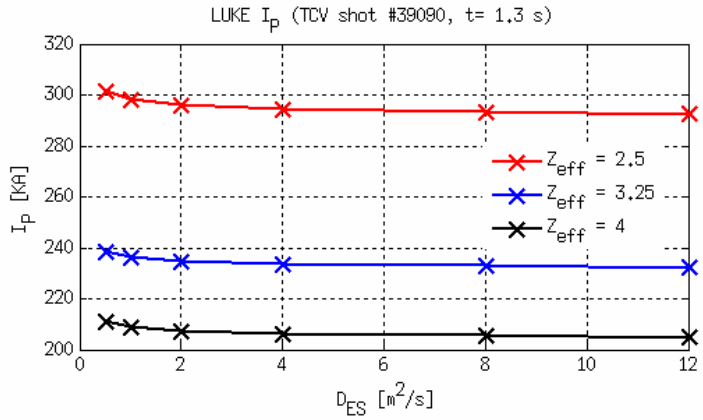

Figure 10. Influence of the effective charge ($Z_{\rm eff}$) and fast electron diffusivity (D_{ES}) on the total driven current (I_p) calculated by LUKE for TCV shot 39090. The equilibrium parameters are taken at $t = 1.3$ s when the experimental value of $Z_{\rm eff}$ is 3.25; the experimental $I_p = 230$ kA at this time is well recovered in the simulation.

following ratio:

$$\Delta\mathrm{HXR}_{\rm syn} = \frac{\mathrm{HXR}_{[2^{\rm nd},3^{\rm rd}]} - (\mathrm{HXR}_{[2^{\rm nd}]} + \mathrm{HXR}_{[3^{\rm rd}]})}{\mathrm{HXR}_{[2^{\rm nd}]} + \mathrm{HXR}_{[3^{\rm rd}]}}. \tag{6}$$

To exclude effects directly due to variations in plasma parameters, we now keep the plasma equilibrium and experimental profiles fixed, using experimental data at $t = t_X = 1.3$ s. In other words, only the vacuum magnetic field and plasma current are varied in time. Not shown explicitly in Eq. (6) for simplicity of notation is the

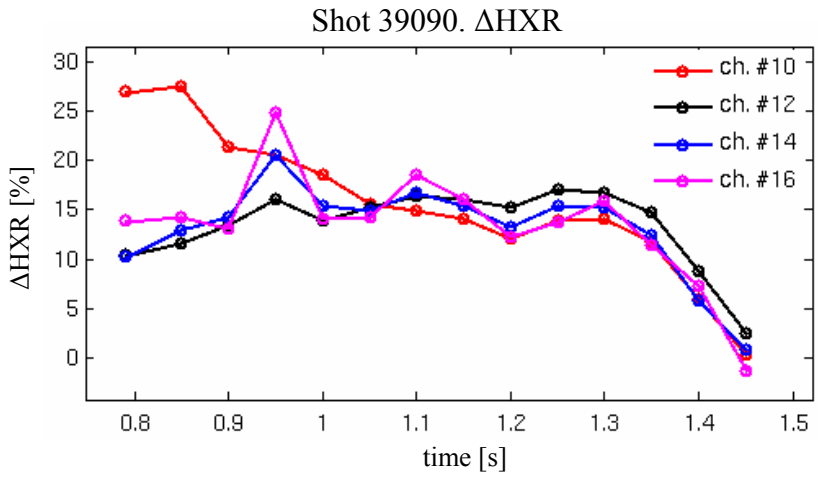

Figure 11. TCV shot 39090: synergistic HXR variation calculated by LUKE/R5-X2 for the energy range 16–40 keV on chords 10, 12, 14 and 16. $D_{ES} = 0.5$ m^2/s.

subtraction from each term of the background emission in the absence of any EC heating (the thermal bulk contribution).

In figure 11 the value of $\Delta\text{HXR}_{\text{syn}}$ is shown for a few chords. The signal increase is ∼15% for chords (#12–16) viewing the plasma tangentially from mid-radius (#12, where the EC wave is absorbed) to the plasma core (#16); $\Delta\text{HXR}_{\text{syn}}$ decreases monotonically in time (from 27% at 0.8 s down to 12% at 1.2 s) on chords viewing the periphery of the plasma (#10). A minor peak around $t_X = 1.3$ s is present on all chords. The value of ΔHXR abruptly decreases afterwards, essentially vanishing at 1.45 s, when the 2$^{\text{nd}}$ harmonic is very weakly absorbed in the plasma edge ($\rho \sim 0.75$) and no longer contributes significantly to the suprathermal population needed for the synergy.

6.3. Investigation of possible signatures of synergy

We now examine the crucial question of whether an experimental signature of the synergy has been detected. The minor peaks observed in the experimental HXR emission as a function of time on the more peripheral chords (section 5, also figure 12(a)) must be investigated individually to determine whether they may be related to the synergistic effect we are studying. The simulated HXR signal (figure 12(b)) indeed also shows a secondary peak at $t \sim 0.95$ s on chords #11 and #12. However, this peak is unrelated to synergy because it is present even in simulations with only 2$^{\text{nd}}$ harmonic absorption. Further analysis reveals that this peak coincides, in fact, with a maximum in the experimental Z_{eff} (which of course is one of the inputs to the FP solver). By imposing a constant $Z_{\text{eff}} = 3$ in the simulations, this peak disappears (figure 12(c)). At $t \sim 1.3$ s (the time at which the nominal 2$^{\text{nd}}$ and 3$^{\text{rd}}$ harmonic absorption layers coincide), a peak in the HXR simulated profile is present for chords #9 to #13. This peak also exists in simulations with only 2$^{\text{nd}}$ harmonic absorption; thus it, too, cannot be related to synergistic effects.

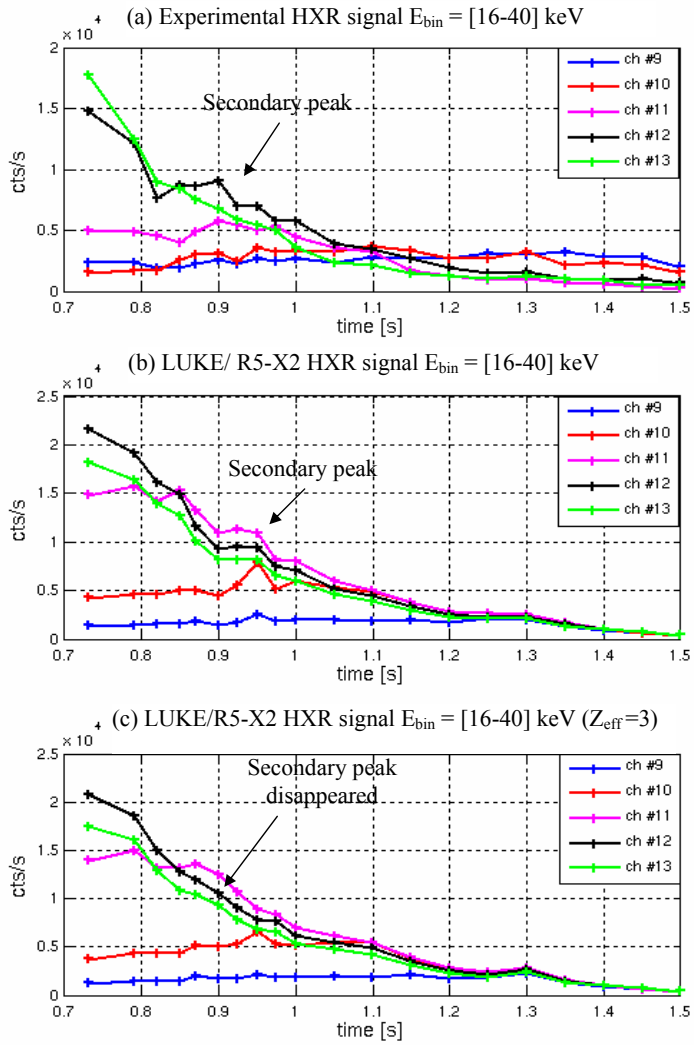

Figure 12. (a) Experimental vs (b) simulated HXR profiles in energy range 16–40 keV for TCV shot 39090. In (c) the simulation has been repeated with a constant $Z_{\rm eff} = 3$. The LUKE simulations are performed with a fast electron radial diffusivity $D_{ES} = 0.5$ m^2/s.

The issue of whether local peaks can be expected in the HXR signals vs time as a result of synergy can be addressed in an alternative way. Here, we freeze the magnetic equilibrium and the input profiles at a given time (here at $t = t_X = 1.3$ s; $Z_{\rm eff} = 3.25$; $D_{ES} = 0.5$ m^2/s) and scan the power deposition location radially by artificially varying the EC beam frequency. In this way the influence of variations in $Z_{\rm eff}$, density and temperature is eliminated. By covering the 79–84 GHz frequency range we can emulate shot 39090, with the dominant 2$^{\rm nd}$ harmonic deposition radius spanning the range from $\rho_V = 0.5$ to $\rho_V = 0.74$. As shown in figure 13, the simulated HXR signal behaves similarly, peaking at the same frequencies on the different chords, whether the 3$^{\rm rd}$ harmonic absorption is taken into account or not: no visible synergy signature is detected.

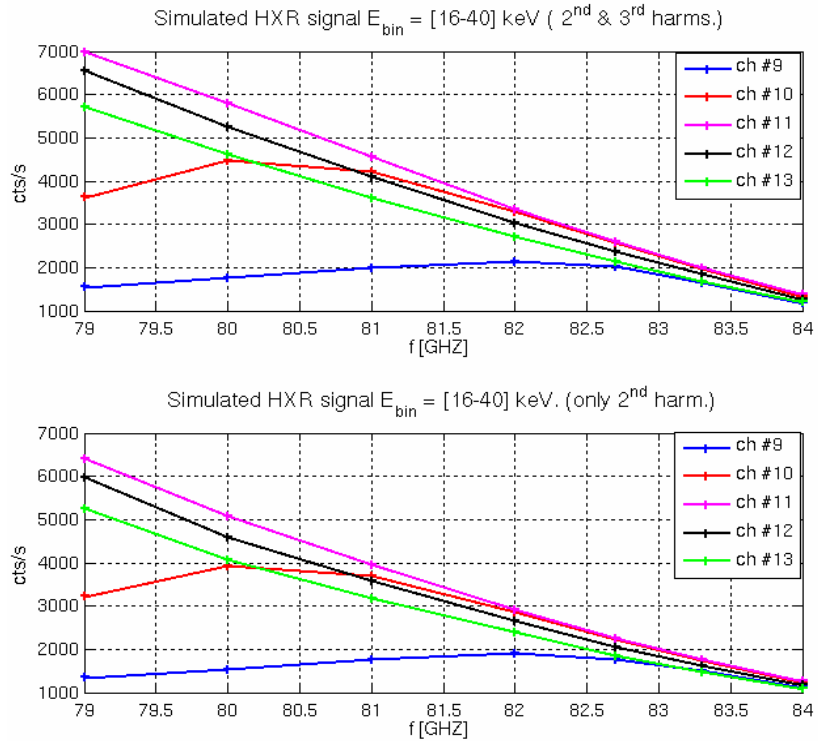

Figure 13. Calculated HXR signals in the 16–40 keV energy range, for several chords, from LUKE/R5-X2 simulations with EC frequency scan (79–84 GHz). Equilibrium profiles taken from TCV shot 39090 at $t = 1.3$ s ($Z_{\rm eff} = 3$, $D_{ES} = 0.5$ m^2/s).

7. Perspectives for synergy detection

A direct detection of a synergy effect could strictly only come from a direct comparison with a control case, i.e., a scenario in which the possibility of synergy is removed but all other experimental conditions are unchanged, including the separate absorption of 2nd and 3rd harmonic waves. This would be a difficult proposition under any circumstances but is specifically not possibile in the present setup. Such an experiment could conceivably be arranged with 2nd and 3rd harmonic heating at different frequencies, as in such a case the two heating sources can be turned on and off separately.

Convincing indirect evidence could be provided by a clear peak in the time dependence of a key signal during, e.g., a magnetic-field ramp, provided it could not be imputed to plasma parameter changes and provided it occurred at a time at which a break in monotonicity was theoretically expected to occur. Such a key signal in our case is the HXR emission, but we have determined in the previous section that its local increases during the magnetic-field ramp could not be ascribed to an increase in synergy.

Lacking such clear evidence, only a very good match between predicted and measured HXR emission, beyond the error bars, could be construed as corroborating the existence of a synergy effect. The quantitative mismatches described in section 6.2, however, are proof of imperfections in the model and thus rule out this possibility also.

We may nevertheless ask the question of whether any other experimental signature

of synergy can be sought in the HXR data, especially in view of a possible optimised future experimental design. Firstly, in section 7.1, we shall study the sensitivity of the HXR synergistic enhancement on plasma parameters to determine the minimum level that would be detectable beyond the experimental error bars, and compare it with the calculated level. Afterwards, in section 7.2, we shall analyse the dependence of the synergistic enhancement on the ECRH power and on the assumed cross-field diffusivity of suprathermal electrons, and specifically seek the conditions that would maximise the HXR enhancement.

7.1. Sensitivity of synergistic HXR enhancement to plasma parameters

We seek to determine the increase in HXR emission due to synergy, if any, and whether it is experimentally measurable. The question of measurability is examined by splitting the problem in two parts. First, to exclude effects directly due to variations in plasma parameters, we keep the plasma equilibrium and experimental profiles fixed, using experimental data at $t = t_X = 1.3$ s. In other words, only the vacuum magnetic field and plasma current are varied in time. In a second stage, we shall study the dependence on plasma parameters separately. Where not otherwise indicated, the level of fast electron diffusivity used is $D_{ES} = 0.5$ m^2/s.

In particular, the synergy is found to be very sensitive to the electron density. Keeping the normalized density profile fixed, with the experimental shape it has at time $t = t_X = 1.3$ s, and varying the overall density level about the experimental value, we find that $\Delta\mathrm{HXR}_{\mathrm{syn}}$ for all chords (#8–16) is actually maximised at the experimental value (Fig14c,d). Its maximum value is on chord 16 and is equal to 17%. The experimental conditions ($\langle n_e \rangle = 1.5 \times 10^{19}$ m^{-3}), therefore, are particularly favourable. We find, however, that a 10% density variation results in a ∼30% variation in the absolute HXR emission (figure 14a). It should be noted that a 10% density variation is of the same order of magnitude as the experimental error on the local density measured by Thomson scattering and can consequently easily mask any experimental evidence for a $2^{\mathrm{nd}}/3^{\mathrm{rd}}$ harmonic synergy in the HXR emission, which does not exceed 28% (figure 11).

7.2. Dependence of synergistic HXR enhancement on ECRH power and suprathermal electron diffusivity

We address now the effect of the power deposition on the synergy, to determine whether higher injected power could enhance the effect to the point of making it clearly measurable. Once again, we fix the magnetic equilibrium and the input profiles to the Fokker-Planck code, taking them from experimental data at $t = t_X = 1.3$ s, and we artificially increase the injected EC power. We also repeat this operation for different values of the fast electron radial diffusivity D_{ES} from 0 to 5 m^2/s. The results of this series of simulations are shown in figure 15.

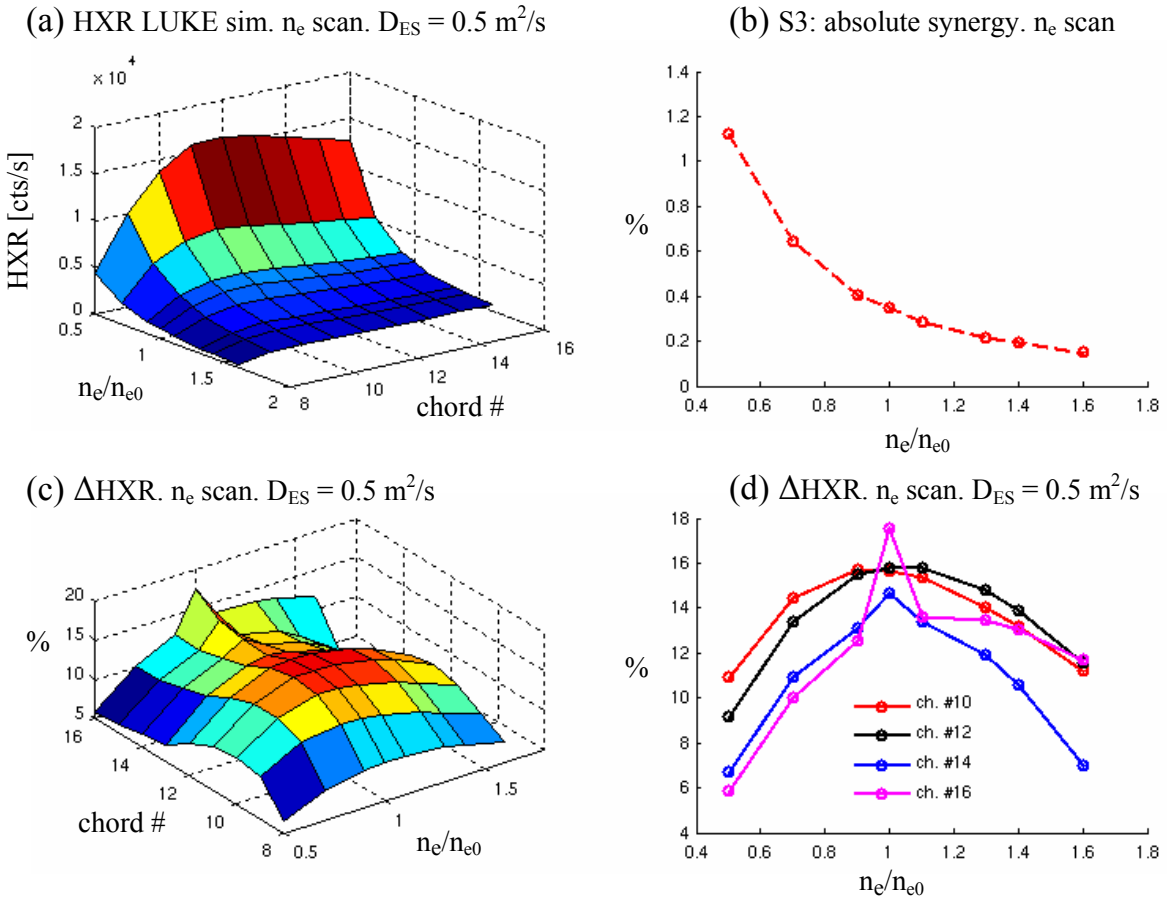

Figure 14. TCV shot 39090: calculated synergy dependence on plasma density, with equilibrium profile shape taken at $t = 1.3$ s: (a) predicted HXR emission to be measured by the vertically viewing camera as a function of normalized density n_e/n_{e0}; (b) absolute synergy S_3; (c-d) synergistic variation $\Delta\text{HXR}_{\text{syn}}$. All plots refer to the energy range 16–40 keV. A radial diffusivity 0.5 m^2/s is assumed.

The synergistic gain in the HXR emission initially grows with power for all the values of D_{ES} considered. At higher injected power, the quasilinear flattening of the electron distribution function begins to play an important role, reducing the dominant 2nd harmonic absorbed fraction, which ultimately also reduces the excess fast electron population attributable to the 3rd harmonic. This translates in a degradation of $\Delta\text{HXR}_{\text{syn}}$ with power beyond a given threshold. We remark that by increasing the level of fast electron radial transport (a higher level of transport arguably being reasonable with increased P_{abs}, and providing a better match to the experimental HXR profile as seen in section 6), the decrease of $\Delta\text{HXR}_{\text{syn}}$ begins at higher injected power (figure 15(a)). Additionally, the absolute value of $\Delta\text{HXR}_{\text{syn}}$ increases with the diffusivity. An inspection of the distribution function dynamics suggests that this is due to the greater spatial overlap between the effective resonant regions for the two harmonics.

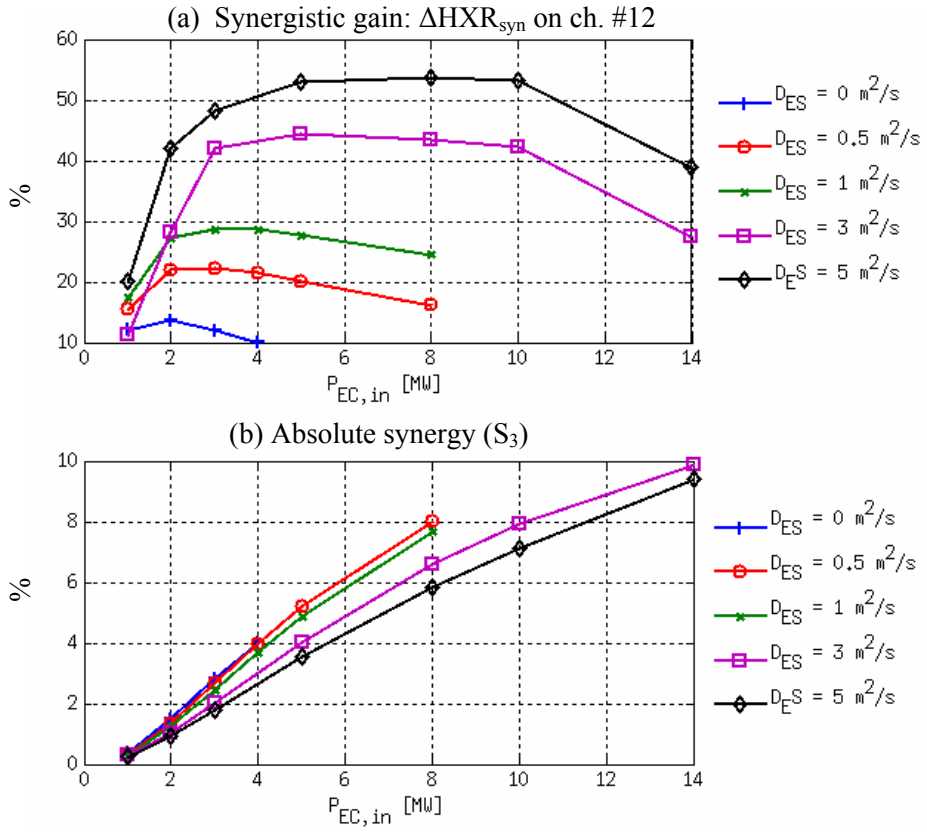

Figure 15. TCV shot 39090, equilibrium profiles taken at $t = 1.3$ s: (a) synergistic HXR variation for chord #12 and (b) absolute level of synergy (S_3) as functions of the injected EC power for different levels of fast electron radial diffusivity. All calculations by LUKE/R5-X2 for the energy range 16–40 keV.

However, the significant flattening of the distribution function at high power actually results in a *decrease* of the absolute level of power absorption synergy S_3 with diffusivity, as shown in figure 15(b), even as the fast electron population is enhanced. Also, S_3 increases linearly with the injected power, confirming and extending the result shown in figure 6.

If independent experimental evidence were provided of a sufficiently high level of diffusivity and the injected power could be increased substantially, it would be possible in principle to reach values of $\Delta\text{HXR}_{\text{syn}}$ in excess of 30%, which should considerably facilitate the detection of synergy. This level of power, however, is not currently attainable in our configuration on TCV, since the required equatorial injection limits the maximum injected power to 1 MW. More fundamentally, the predicted HXR emission level depends strongly on the transport level and even on the details of the transport model, which can be studied experimentally only in limited and semi-quantitative fashion. An unequivocal confirmation of a synergy effect would then, once again, require a hypothetical direct comparison of scenarios with and without synergy, with otherwise identical plasma parameters.

8. Conclusions

A study of the interplay between 2nd and 3rd harmonic EC wave absorption at the same frequency, both experimentally in the TCV tokamak and through numerical modelling, has been discussed in this paper. The TCV experimental configuration enables the simultaneous absorption of the injected EC wave at two different harmonics in the plasma: the 2^{nd} harmonic on the HFS and the 3^{rd} harmonic on the LFS of the magnetic axis. Extensive simulations with the LUKE Fokker-Planck code have evidenced an enhanced 3^{rd} harmonic absorption in the presence of 2^{nd} harmonic heating. This enhancement is mediated by the presence of a significant suprathermal electron population generated by the 2^{nd} harmonic electron acceleration. Complex conditions of alignment for the wave-particle interactions in both physical space and velocity space must be met for the synergy to occur. The assumed level of cross-field fast electron transport is also found to have a significant influence on the synergy. The process of characterizing these conditions has shed light on the fundamental processes underlying high-power EC wave-particle interactions.

Because of the intrinsically poor 3^{rd} harmonic absorption, no direct measurement of the 3^{rd} harmonic absorption, much less of any synergistic enhancement, is possible. The HXR emission has been investigated as a possible candidate for the indirect manifestation of a possible synergy. The predicted synergistic HXR enhancement in the TCV experimental conditions however is modest, i.e. less than 20%, precluding an unequivocal detection, since such a variation can be easily masked by fluctuations in the electron density and effective charge. More fundamentally, the uncertainties in the model, including - critically - the nature and level of suprathermal electron transport, preclude an unambiguous quantitative comparison even in more extreme conditions (higher power and higher diffusivity) in which a stronger HXR enhancement could theoretically occur. The nature of the experimental setup employed in this study also excludes a direct comparison with and without synergy in the same conditions.

Nevertheless, the current state of research on the fundamentals of wave-particle interaction gives reasons for cautious optimism. Adequate simulation tools are now available in support of these studies, and in particular the understanding that stems from the analysis presented in this paper is a solid starting point for the design of new, optimised experimental scenarios. The subtle effects of inter-harmonic synergy, among others, may well still be open to experimental investigation.

Acknowledgments

This work, supported by the European Communities under the contract of Association between EURATOM and CEA, was carried out within the framework of the European Fusion Development Agreement. The views and opinions expressed herein do not necessarily reflect those of the European Commission. This work was also supported in part by the Swiss National Science Foundation.

Appendix A. Phase space analysis of 2^{nd}-3^{rd} harmonic ECRH absorption synergy

In this Appendix the mechanisms underlying the evolution of the synergistic 3^{rd} harmonic absorption enhancement in the magnetic-field sweep of shot 39090 are examined in detail. We shall discuss first the case without spatial transport: synergy can then only occur for a flux surface and class of electrons for which the two resonances coincide.

The early 3^{rd} harmonic peak ($t < 1$ s in simulations with 2^{nd} and 3^{rd} harmonics; figure 5, left column) can only be explained by 3^{rd} harmonic absorption on the high energy tail of the electron distribution function generated as a consequence of the 2^{nd} harmonic heating. The nominal (cold) 3^{rd} harmonic resonant layer indeed is not even inside the plasma at these times. The presence of a significant suprathermal electron tail generated by the 2^{nd} harmonic absorption is an essential ingredient for this synergy.

In figure A1, the momentum space dynamics are analysed for the case $t = 0.82$ s; the 2^{nd} and 3^{rd} harmonic interaction is maximized at large values of the total momentum ($p/p_{Te} \sim 8$) in the core ($\rho < 0.5$) where a large distortion in the electron distribution function $f(p)$ is seen. Moving to larger radii (right column in figure A1), the 3^{rd} harmonic interaction moves to regions of lower momentum, whereas the 2^{nd} harmonic interaction occurs mainly on a highly energetic ($p/p_{Te} \sim 10$) but poorly populated part of the electron distribution function, reducing the opportunities for synergy.

The nominal 3^{rd} harmonic resonant layer enters the plasma, from the LFS, at $t \sim 1$ s (as shown in figure 5) and moves to inner radial positions afterwards ($\rho_V \sim 0.58$ at $t = 1.5$ s). Synergistic 2^{nd} /3^{rd} harmonic interaction is found to occur at radial locations where electrons resonating at the 2^{nd} and 3^{rd} harmonic have similar energies in a sufficiently populated part of the distribution function. In addition, a significant synergy requires that the interaction takes place on the LFS of the nominal 2^{nd} harmonic resonance, which is the most efficient means of generating a suprathermal tail as the resonant electrons are less collisional, and the power is highest as we inject from the LFS. Also the high rate of pitch-angle scattering makes these electrons available for resonant X3 interaction preferentially on the HFS of the nominal 3^{rd} harmonic resonance. This complex interplay creates relatively favourable conditions for the synergy throughout the first part of the scan up to the point of radial alignment between the nominal resonances at $t = 1.3$ s. The maximum of the absolute synergy S_3 occurs indeed at $t = 1.3$ s where a fair overlap of the two absorption regions in velocity space is observed at $\rho \sim 0.7$ (slightly inside the cold resonance location), as seen in figure A2. At later times the condition that the resonant electrons be on the HFS of the 3^{rd} harmonic and on the LFS of the 2^{nd} implies an increasing Doppler up-shift for the latter, i.e., a large parallel velocity and therefore a rapidly vanishing population. The synergy accordingly drops rapidly for $t > 1.3$ s.

When transport is considered (figure A3), the radial propagation of electrons increases the opportunities for the interaction between the two resonances. The

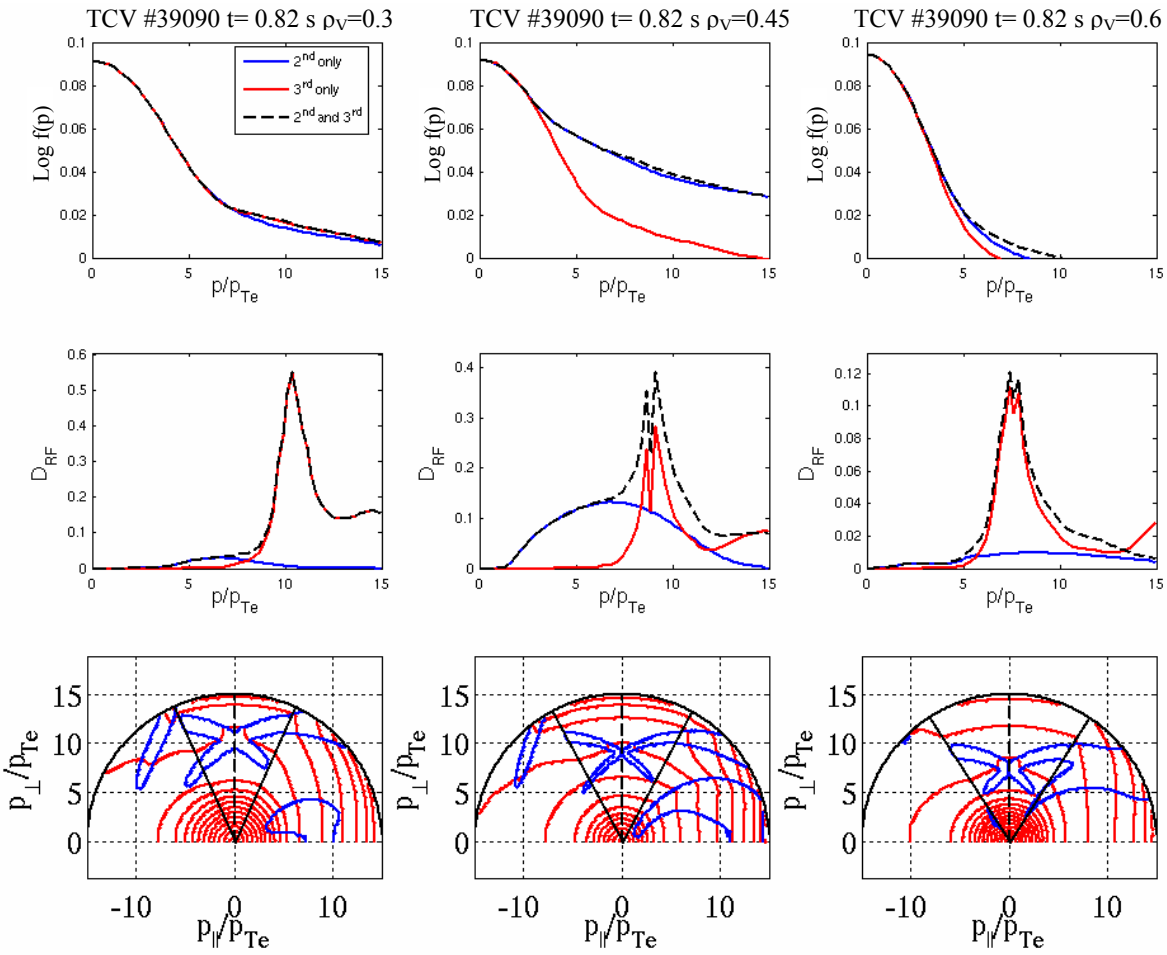

Figure A1. Electron distribution function $f(p)$ for TCV shot 39090 at $t = 0.82$ s as a function of the total momentum, first row; RF diffusion coefficient (D_{RF}, the norm of the diffusion tensor) as a function of the total momentum, middle row; 2D momentum space representation of $f(p)$ (red), $D_{RF} \neq 0$ contours (blue), third row. The three columns refer to three different radial positions. The wave-particle interaction occurs in velocity space where $D_{RF} \neq 0$. The total momentum is normalized to the thermal momentum, defined as $p_{T_e} = m_e v_{T_e}$.

3rd harmonic radial deposition profile is accordingly broadened. This effect is more pronounced when the 3rd harmonic absorption occurs at inner radii (and at higher energy for $t < 1$ s). The result is, however, a stronger flattening of the distribution function and, somewhat paradoxically, a decrease in absolute synergy (figure 6, red curves). In the present study, fast electron radial transport is modelled with an electrostatic (ES) model, whereby a radially uniform and energy-independent radial diffusion coefficient (D_{ES}) is applied to fast electrons with $v_e \geq 3.5\, v_{Te}$. As discussed in section 6.2, the strongest constraint on the diffusivity is provided by the requirement of a minimal discrepancy between experimental and calculated HXR profiles, which suggests the value $D_{ES} = 0.5$ m^2/s at the crossing time, 1.3 s, although the optimal value varies during the discharge.

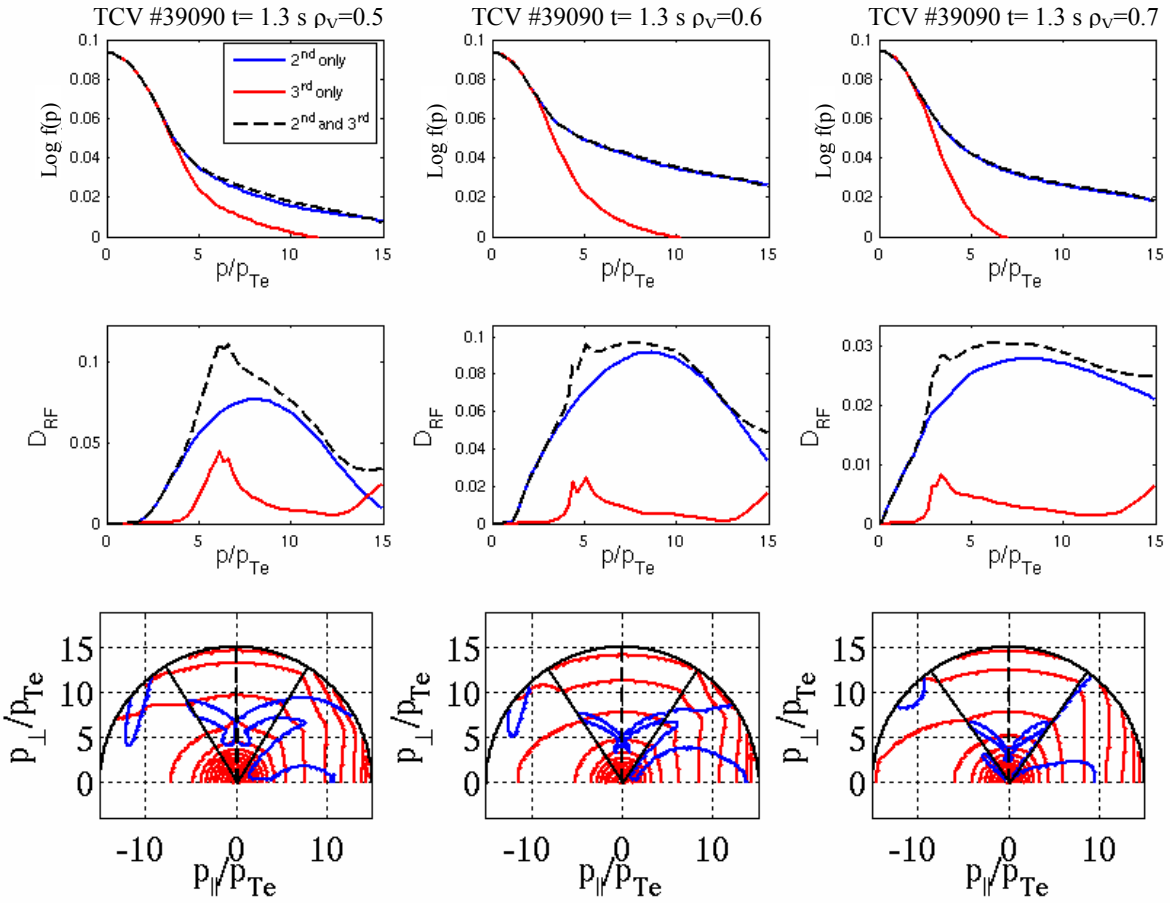

Figure A2. Electron distribution function $f(p)$ for TCV shot 39090 at $t = 1.3$ s as a function of the total momentum, first row; RF diffusion coefficient (D_{RF}, the norm of the diffusion tensor) as a function of the total momentum, middle row; 2D momentum space representation of $f(p)$ (red), $D_{RF} \neq 0$ contours (blue), third row. The three columns refer to three different radial positions. The wave-particle interaction occurs in velocity space where $D_{RF} \neq 0$. The total momentum is normalized to the thermal momentum, defined as $p_{T_e} = m_e v_{T_e}$

References

[1] Erckmann V and Gasparino U 1994 *Plasma Phys. Control. Fusion* **36** 1869
[2] Lloyd B 1998 *Plasma Phys. Control. Fusion* **40** A119
[3] Prater R 2004 *Phys. Plasmas* **11** 2349
[4] Zohm H *et al* 2007 *Nucl. Fusion* **47** 228
[5] Goodman T P *et al* 2011 *Phys. Rev. Lett.* **106** 245002
[6] Coda S *et al* 2003 *Nucl. Fusion* **43** 1361
[7] Coda S *et al* 2006 *Plasma Phys. Control. Fusion* **48** B359
[8] Harvey R W *et al* 2002 *Phys. Rev. Lett.* **88** 205001
[9] Nikkola P *et al Nucl. Fusion* 2003 **43** 1343
[10] Decker J and Peysson Y 2004 Report EUR-CEA-FC-1736 Euratom-CEA
[11] Hofmann F *et al* 1994 *Plasma Phys. Control. Fusion* **36** B277
[12] Goodman T P and the TCV Team 2008 *Nucl. Fusion* **48** 054011
[13] Alberti A *et al* 2002 *Nucl. Fusion* **42** 42

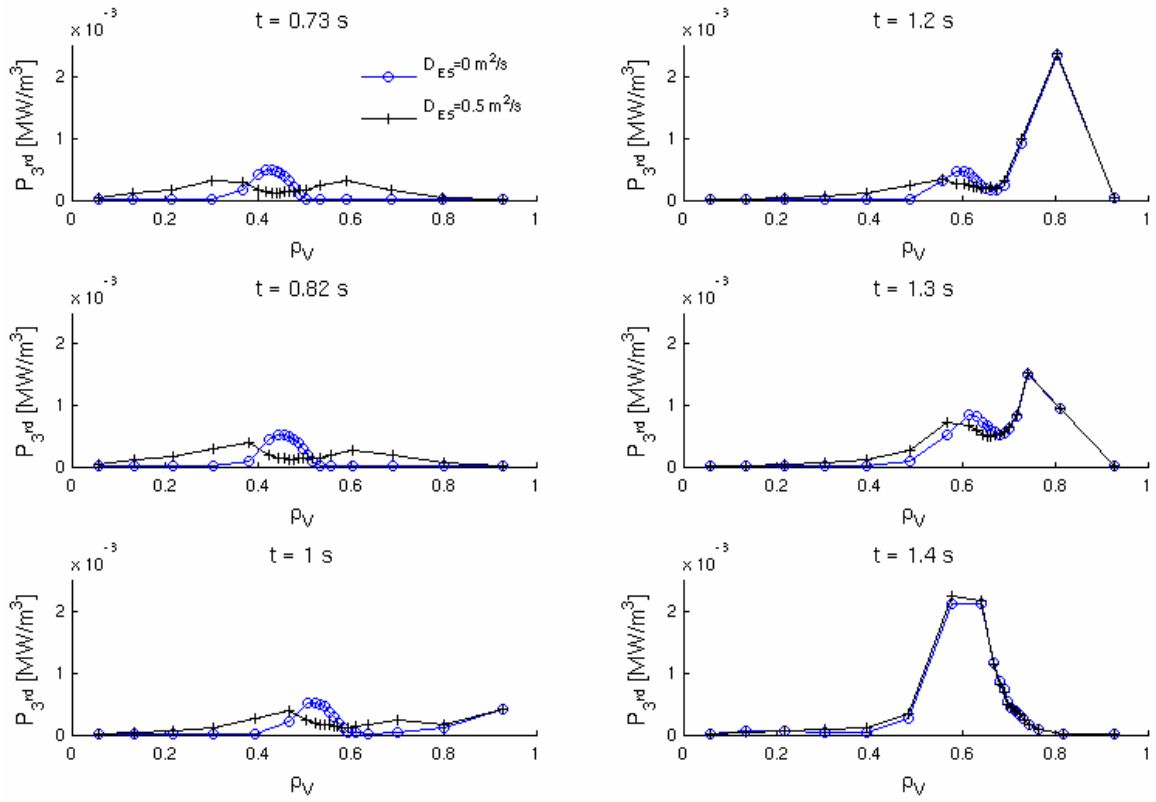

Figure A3. Effect of fast electron radial transport on the radial power deposition profiles for the 3rd harmonic (with all harmonics included in the calculation), TCV shot 39090. Blue curves: no transport; black curves: radial diffusivity 0.5 m^2/s.

[14] Blanchard P *et al* 2002 *Plasma Phys. Control. Fusion* **44** 2231
[15] Manini A *et al* 2002 *Plasma Phys. Control. Fusion* **44** 139
[16] Coda S 2008 *Rev. Sci. Instrum.* **79** 10F501
[17] Peysson Y, Coda S, Imbeaux F 2001 *Nucl. Instr. and Methods in Phys. Res. A* **458** 269
[18] Peysson Y and Imbeaux F 1999 *Rev. Sci. Instrum.* **70** 3987
[19] Peysson Y and Decker J 2008 Report EUR-CEA-FC-1739 Euratom-CEA
[20] Peysson Y and Decker J 2008 *Phys. Plasmas* **15** 092509
[21] Hofmann F and Tonetti G 1988 *Nucl. Fusion* **28** 1871
[22] Decker J *et al* 2010 *Phys. Plasmas* **17** 112513
[23] Rax J M and Moreau D 1989 *Nucl. Fusion* **29** 1751